Reaction Chemistry & Engineering

Magnetic Separation of Immobilized Biocatalyst Enables Continuous Manufacturing with a Solids-Forming Reaction

Journal:	*Reaction Chemistry & Engineering*
Manuscript ID	RE-ART-04-2023-000214.R1
Article Type:	Paper
Date Submitted by the Author:	26-May-2023

Complete List of Authors:	Lagerman, Colton; Georgia Institute of Technology, School of Chemical & Biomolecular Engineering Marshall, Grant; Georgia Institute of Technology, School of Chemical & Biomolecular Engineering McDonald, Matthew; Georgia Institute of Technology, School of Chemical & Biomolecular Engineering Harris, Patrick; Georgia Institute of Technology, School of Chemical & Biomolecular Engineering Grover, Martha; Georgia Institute of Technology, School of Chemical & Biomolecular Engineering Rousseau, Ronald; Georgia Institute of Technology, School of Chemical & Biomolecular Engineering Bommarius, Andreas; Georgia Institute of Technology, Chemical & Biomolecular Engineering

ARTICLE

Magnetic Separation of Immobilized Biocatalyst Enables Continuous Manufacturing with a Solids-Forming Reaction

Received 00th January 20xx,
Accepted 00th January 20xx

DOI: 10.1039/x0xx00000x

Colton E. Lagerman[a]†, Grant D. Marshall[a]†, Matthew A. McDonald[a], Patrick R. Harris[a], Martha A. Grover[a], Ronald W. Rousseau[a], Andreas S. Bommarius*[a]

End-to-end continuous manufacturing often provides improvements to product quality control and process economics over traditional batch processes. Design of new continuous unit operations for product isolation and catalyst recovery is necessary for realization of fully continuous processes involving difficult or coupled chemistries and separations. In this work, a magnetic separation technique is designed and applied to separate biofunctionalized catalyst particles from crystalline product in a continuous process to yield a high-purity product stream and continuously recycle catalyst to a reactor. A separator was created to recover and recycle > 99.9% of catalyst in a continuous reactive crystallizer. The separator is demonstrated for enzymatic synthesis of amoxicillin, yielding pure amoxicillin trihydrate with a volumetric productivity of > 250 g/L/day. Magnetic separation systems are envisioned to enable other continuous, heterogeneously catalyzed, solids-forming reactions.

1. Introduction

Continuous manufacturing offers several advantages over batch-wise processes, including increased system control and reduced variation in product quality, and could provide substantial improvements for larger manufacturing processes in the pharmaceutical arena [1-6]. The success of recent efforts to move commercial production, at least in part, to a continuous setup is promising [1, 5, 7-14], but additional work is needed. Design of new, continuous unit operations will enable end-to-end continuous manufacturing, especially for challenging chemistries such as the solids-catalyzed, solids-forming reactions emphasized in this study. Biocatalysts also complement continuous manufacturing by enabling difficult chemistries with their unmatched specificity and selectivity.

β-lactam antibiotics, the most widely used antibiotics class in the world, are one focus for new biocatalytic and continuous processes. Manufacturing of β-lactam antibiotics has been geographically concentrated which has led to supply chain issues and critical shortages throughout the world, including amoxicillin shortages in Europe and the United States announced as recently as October 2022. Expanding both how and where such life-saving medicines can be produced could prevent future shortages [12].

The present study was motivated by the continuous reactive crystallization of β-lactam antibiotics, whereby penicillin G acylase (PGA) converts solution-phase reactants into target product that subsequently forms needle-shaped crystals (Scheme 1) [15-18]. Reactive crystallizations are processes in which supersaturation is generated from a solution-phase reaction, providing the driving force for crystallization [19]. Generally, reactive crystallization can be useful for process intensification [20], overcoming unfavorable reaction equilibria [18], and for isolation of desired intermediates as in the case of PGA-catalyzed β-lactam synthesis [10, 15, 18, 20-31]. The formation of solid product directly from solution-phase reactants provides increased selectivity in β-lactam production.

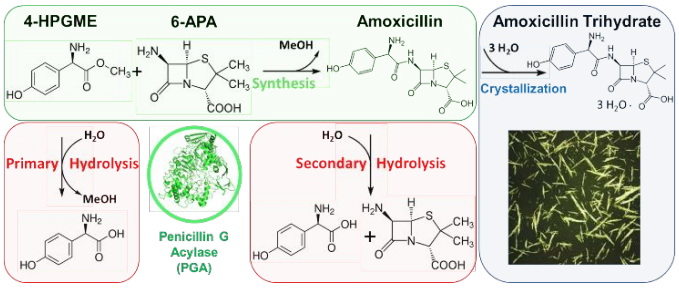

Scheme 1. Reactive crystallization of amoxicillin trihydrate catalyzed by penicillin G acylase (PGA).

For many enzymatic reactions, immobilized enzyme is beneficial for increased enzyme stability and reuse, prevention of protein impurity in the final active pharmaceutical ingredient (API), use in a wider array of solvents, and ease of implementation in continuous processing [32, 33]. In addition, for low-value, high-volume pharmaceuticals such as β-lactam antibiotics, the cost of enzyme isolation and purification can be mitigated in part by immobilization. However, for enzyme-catalyzed reactive crystallizations, separation of solid, immobilized biocatalyst and solid, crystallizing product poses a difficult and unsolved problem. This problem extends to other heterogeneously catalyzed reactions where a solid product is ultimately desired [19].

The use of density-based and size-based separations have previously been studied; however, such designs often complicate mixing, have long settling times, or require complex and costly,

[a] School of Chemical and Biomolecular Engineering, Georgia Institute of Technology, Atlanta, GA 30332

† Footnotes relating to the title and/or authors should appear here.

Electronic Supplementary Information (ESI) available: [details of any supplementary information available should be included here]. See DOI: 10.1039/x0xx00000x

careful control of particle size. Maintaining a robust difference in particle size either requires milling or catalyst particles that are much larger than the crystals [34]. For catalytic particles, increased size typically results in reduced performance and mass-transfer limitations [35, 36]. To avoid these issues, the addition of bead magnetic properties provides an additional variable to manipulate the separation design. Magnetic separation has been implemented in cell separation [37-39], DNA isolation [40], and iron ore isolation [41]; however, examples of continuous magnetic separation or magnetic separation of typical immobilized catalyst and crystal sizes (10 – 1000 µm) are rare. Previous studies using magnetic separation for recovery of immobilized biocatalysts in magnetic nanoparticles for biocatalysts [42, 43] and palladium catalysts [44] as well as magnetic microparticles for biocatalysts [45] have been demonstrated but focused solely on recovery from solution-phase products. In this work, magnetic separation is used for both catalyst recovery and product isolation simultaneously.

In this study, a continuous magnetic separator was designed and applied to continuously remove catalytically functionalized magnetic spheres from a slurry of crystalline product with high separation efficiency and product purity on a ~100 g/day scale. The device was rapidly prototyped using 3D printing and neodymium magnets. The final 3D printed device is a low-cost system that can be parallelized or used in series for enhanced separations. The device design was detailed using computational fluid dynamics (CFD), magnetic field simulations, and separation ability in both single- and dual-device configurations in series for a wide range of particle sizes. Finally, we demonstrate recovery and continuous recycle of immobilized biocatalyst during an 11-hour enzymatic reactive crystallization to isolate highly pure amoxicillin trihydrate generated biocatalytically from magnetic agarose particle-bound PGA.

2. Experimental

2.1 Initial system characterization

The velocities of paramagnetic particles with diameters between 212-250 µm (Cospheric, Santa Barbara, CA) were tracked using slow motion video analysis as they settled to the bottom of a cuvette in the presence of a magnetic field to calculate relevant forces in the system. The experiment was repeated in 3 different solutions with different viscosities to validate results. The experiment was video recorded with an iPhone camera, and the velocity was calculated by plotting particle displacement after each frame. The velocities of at least 10 particles were plotted against distance from the magnet surface under the cuvette. The force balance model, shown below, was fit to the data to determine an estimate of the particle magnetization, *m*, and calculate ratios of forces in the system. Simulations of the magnetic field generated by two N52 neodymium magnets (Figure S2) were used to calculate the magnetic dipole moment (Figure S3) of 212 µm diameter magnetic particles used in the settling experiments. Calculating the forces present in the system was an important step to determine the separator design.

$$\sum F = 0 = F_g + F_M - F_B - F_D \#(1.1)$$

where F_g is the gravitational force, F_M is the magnetic force, F_B is the buoyancy force, and F_D is the drag force. Solving the force balance,

$$0 = \rho_p g\left(\frac{\pi {d_p}^3}{6}\right) + (m \cdot \nabla)B - \rho_f g\left(\frac{\pi {d_p}^3}{6}\right) - C_D \rho_f \left(\frac{\pi {d_p}^2}{4}\right)\left(\frac{u^2}{2}\right) \#(1.2)$$

where the drag coefficient C_D is assumed to equal $24/Re$ which gives a settling velocity of

$$u_s = \frac{g\, {d_p}^2(\rho_p - \rho_f)}{18\, \mu_f} + \frac{(m \cdot \nabla)B}{3\, \pi\, d_p\, \mu_f} \#(1.3)$$

2.2 Separator design and testing

SOLIDWORKS computer automated design software was used to design the devices and simulate fluid and particle flow within them. Stereolithographic printing with detail of 50 µm of glass fiber impregnated resin afforded durable, high-detail prototypes. For a final device a bio-pharmaceutical-compatible resin should be used; however, for initial testing this was unnecessary. For initial separator design inert paramagnetic and non-magnetic polyethylene spherical beads measuring 212–250 µm in diameter were studied, and later iterations used 53–63 µm in diameter beads (Cospheric, Santa Barbara, CA). The larger beads were used in initial experiments as individual beads are discernable, the smaller beads were used to simulate the available sizes of functionalized beads used in a biocatalysis reactor demonstration.

A brief description of the device testing procedure is given below. An Ismatec Reglo ICC peristaltic pump is used to control the flow rates to all but one of the device connections, with the flow rate through the final connection being governed by a mass balance around the device. Beads, 10.0 g/L, suspended in water with 0.01% v/v Triton X-100 surfactant to assist suspension, were pumped through the device at flow rates up to 40 mL/min, depending on the configuration of each device. Crystals were suspended in saturated solution. Magnetic force was generated by N52 grade neodymium magnets. The outlet from the device was collected and flow rate determined gravimetrically. The collected samples were evaporated in an oven and the dry weight of the beads/crystals measured to assess separation factors and selectivity.

As a starting point, the initial device consists of two inlets and two outlets. One inlet feeds solids while the second inlet provides a co-current sweeping stream. While maintaining laminar flow there should be little crossover between streams. The magnetic field gradient pulls magnetic particles out of the feed lane and into the sweep lane. At the outlets the sweep lane is recycled while the feed lane is destined for further downstream processing.

Amoxicillin was used as the model crystal for crystal/biocatalyst separation studies. Amoxicillin is needle-like in shape, with a tendency to form spherulites and agglomerates in high supersaturation. It can grow to > 1000 µm in length but most crystals measure a few hundred µm in length by 10–20 µm in width, giving them an average equivalent spherical diameter of approximately 50 µm. Representative images of the amoxicillin crystals taken *in situ*, as well as the polyethylene beads.

2.3 Computational fluid dynamics simulations

Computational fluid dynamics simulations were conducted with SOLIDWORKS Flow Simulation, an embedded package for SOLIDWORKS 3D CAD software. This aided the iterative design process by streamlining the modeling, simulating, and printing cycle into one application. A key advantage of fluid simulations is lessening the number of design cycles it takes to optimize a separator. SOLIDWORKS Flow Simulation employs time-dependent

Reynolds-averaged 3D Navier-Stokes equations and k-ε turbulence model as the foundations for the fluid simulation. Transient equations are solved by using local time-steps. The software includes boundary layer modeling for laminar, turbulent, and transitional boundary layers. Mesh generation is a crucial step in conducting CFD simulations because it affects the precision and convergence of the solution. SOLIDWORKS generates a basic cubic mesh in the computational region defined by the model geometry, then, this mesh is refined by splitting the basic cell into 8 smaller cells automatically according to the solution gradient or in specified regions such as near the walls of the device. A moderately fine mesh with local refinement near the interior walls of each device was used in each flow simulation.

Inlet and outlet velocities were defined as the primary boundary conditions for the flow simulations because inlet and outlet flow are parameters that can be easily measured and controlled in testing. SOLIDWORKS also requires the user to indicate a pressure boundary condition, so the non-magnetic outlet was always specified at environmental pressure. In each simulation, inlet velocity(s), velocity of the magnetic outlet, and pressure of non-magnetic outlet were specified. SOLIDWORKS Flow Simulation requires the user to define at least one "Goal" for the simulation. These Goals are used for convergence control, stopping criteria for the solver, and to summarize the most important results from the simulation. In each simulation, an Equation Goal was created that required the simulation to provide a solution in which the mass continuity equation was satisfied; That is, the mass flow rate at the inlets minus the mass flow rates at the outlets must equal zero. This also applies to both steady state simulations and to each time step in a time-dependent simulation.

The Particle Study is another utilized feature that simulates the motion of spherical particles injected into the fluid. This provides a prediction of how particles will separate and settle within a device under any given flow condition. Solid and liquid particles can be simulated with specified diameters, material properties, and wall conditions. Although the flow simulation does not support a way to model magnetic influences on certain particles, the gravity constant and particle densities can be manipulated to create a net buoyant or sinking force on the particles approximately equal to the average magnetic force across the width of the device. This method was demonstrated to give an admittedly rough yet sufficient approximation for how magnetic particles move within a device with accommodating geometry. Results from these particle studies are used to estimate the fraction of different types of particles that will appear in each outlet stream and settle within the device.

Two types of CFD simulation were used: steady state and transient flow. Steady state simulations are meant to simulate the ideal separator, with smooth flow and no accumulation of particles. Transient flow was used to simulate the periodic nature of the peristaltic pump used in the physical experiments. Velocity data and particle study results were analyzed to predict how the real device will perform and understand how to improve subsequent designs. Simulations were used in conjunction with physical experiments in an iterative fashion. A device is simulated, it is then evaluated at various flow rates and bead concentrations, observations from experiments are incorporated into the simulations, and finally a new device is designed, simulated, and printed thus restarting the cycle.

2.4 Reactive crystallization of amoxicillin trihydrate

Penicillin G acylase (PGA, EC 3.5.1.11) was immobilized to PureCube Ni-NTA MagBeads XL from Cube Biotech (Monheim, Germany). A total volume of 3 mL of beads were used to immobilize 96 mg PGA. The solids forming reaction from the condensation of 6-aminopenicillanic acid (6-APA, RIA International) with 4-hydroxy phenylglycine methyl ester (4-HPGME, RIA International) to amoxicillin was carried out by continuously feeding 240 mM 6-APA and 300 mM 4-HPGME into a mixed-suspension, mixed-product removal (MSMPR) unit held at 25 °C and controlled to pH 6.3 by dosing in 2 M NaOH. The liquid phase was monitored by high-performance liquid chromatography (HPLC) by collected samples every hour. The solids phase was monitored continuously using Particle Vision and Measurement (PVM, Mettler Toledo) and focused beam reflectance measurement (FBRM, Mettler Toledo). Solid amoxicillin trihydrate generated in the process was dissolved in water to test for purity by HPLC.

3. Results and discussion

The 3D-printed device is shown in Figure 1A. Briefly, slurry is fed into the device inlet before entering an expanded chamber to allow for crystal settling while a magnetic field gradient guides magnetic particles into the top outlet of the device for bead recycling (Figure 1B). The low-volume triangular design allows for a wide range of flow rates (4 to > 20 mL/min) while maintaining reasonable fluid velocity to allow for continuous processing. The magnetic field gradient is generated in the top half of the device using two neodymium magnets placed on either side of the device (Figure 1C). This magnet placement generates a magnetic field such that paramagnetic particles, which respond to gradients in the magnetic field [46], are kept in the upper half of the device (Figures 1B and 1D) due to differences in settling and magnetic forces (Tables S1, S2). Crystals falling to the bottom outlet of the device (Figure 1B) due to settling forces (Figure S1, Table S1) are in the product stream and exit the system for further downstream processing.

The device layout was configured iteratively based on (a) bead property studies through settling experiments, (b) magnetic field and fluid dynamics simulations, and (c) physical testing. SolidWorks Flow Simulation was used to design device dimensions given both solids and liquid characteristics. Magnetic dipole moments were calculated using settling velocities of magnetic particles in liquids having different densities (Figures S2 and S3). From these data, several device designs (Figure S4) were simulated across fluid flow (Figures S6–S11, S13) and magnetic field conditions (Figure 1D) before being printed and tested for separation efficiency of magnetic particles from comparable nonmagnetic particles (Figures S5, S12, S14, S15).

The iterative *in silico* design, print, and test were performed to replicate nonidealities observed in experiments and to identify new designs or operating conditions to correct nonidealities. Two observed nonidealities that were not accounted for in initial simulations were hypothesized to have an adverse effect on the separation: magnetic beads accumulating on the device wall (Figures S6–S8), and sinusoidal fluid velocity introduced by the peristaltic pumps (Figures S9, S10). Bead adhesion to device walls was minimized by engineering the magnetic field gradient to dissipate at the wall and increasing the suspension flow rate. Pump oscillation was minimized by using two synchronized pumps, one for the inlet and one for both outlets so that vortices did not form between the two outlets.

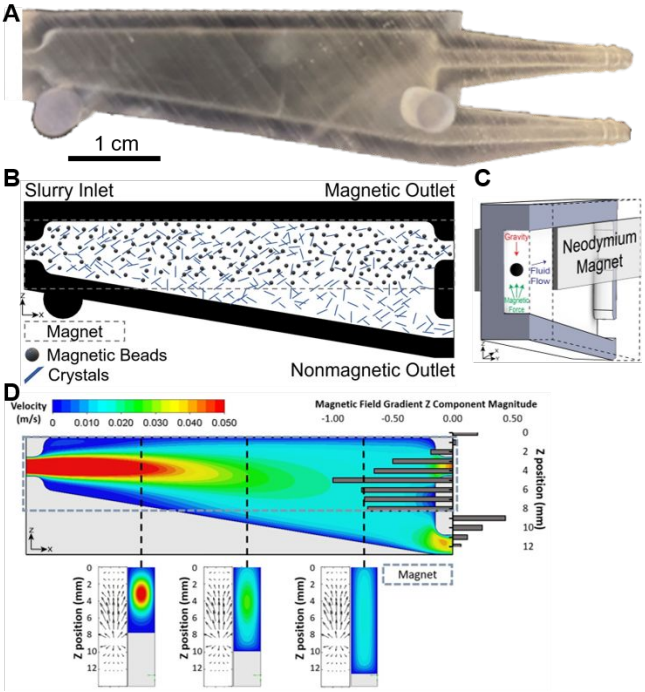

Figure 1. Magnetophoretic separator design and simulation. (A) Photograph of a single separator device (B) Schematic of anticipated flow of particles through the device. Magnetic particles remain above the magnet placement and are funneled to the magnetic outlet (top) while crystals settle out toward the nonmagnetic outlet (bottom). Some fraction of crystals remains distributed throughout the fluid and exit the magnetic outlet with recycled magnetic particles (C) Cross section of device showing placement of neodymium magnets on the top half of the device and the gravitational, magnetic, and fluid flow forces acting on solid particles within the device. (D) Simulation of the separator showing fluid velocity from CFD simulations in the x-direction as well as the magnetic field gradient magnitude generated by placement of magnets on either side of the device. Cross sections (below) show general trends in the x-direction for both magnetic field vectors as well as fluid flow in the x-direction.

The final separator design was tested initially with several bead types and inlet flow rates to determine the operating points for the device. Bead retention (the fraction of beads exiting the top, magnetic outlet) was measured for each slurry of magnetic and nonmagnetic beads having an average diameter of either 60 µm or 212 µm. The fraction of nonmagnetic and magnetic beads present in the magnetic outlet of the device are shown for both 212-µm bead and 60-µm bead experiments (Figure 2A). The 212-µm diameter beads were easier to separate with > 99.5% of all magnetic beads exiting the magnetic outlet at all flow rates studied. However, separation efficiency of the smaller magnetic particles was 96% exiting the magnetic outlet at 6 mL/min and decreasing to 80% at 12 mL/min. Overall, magnetic bead retention decreased with increasing flow rate into the device, and larger beads were easier to separate than smaller beads. These observations are likely due to the balance between the magnetically induced velocity of the particles upward relative to both the fluid velocity carrying particles forward and gravity pulling particles downward [47]. In addition, the fraction of nonmagnetic beads exiting the magnetic outlet was between 40 – 70% (Figure 2A) except at the lowest flow rates.

A similar trend occurs with separation of 60 µm magnetic beads from amoxicillin crystals. The highest solids retention occurred

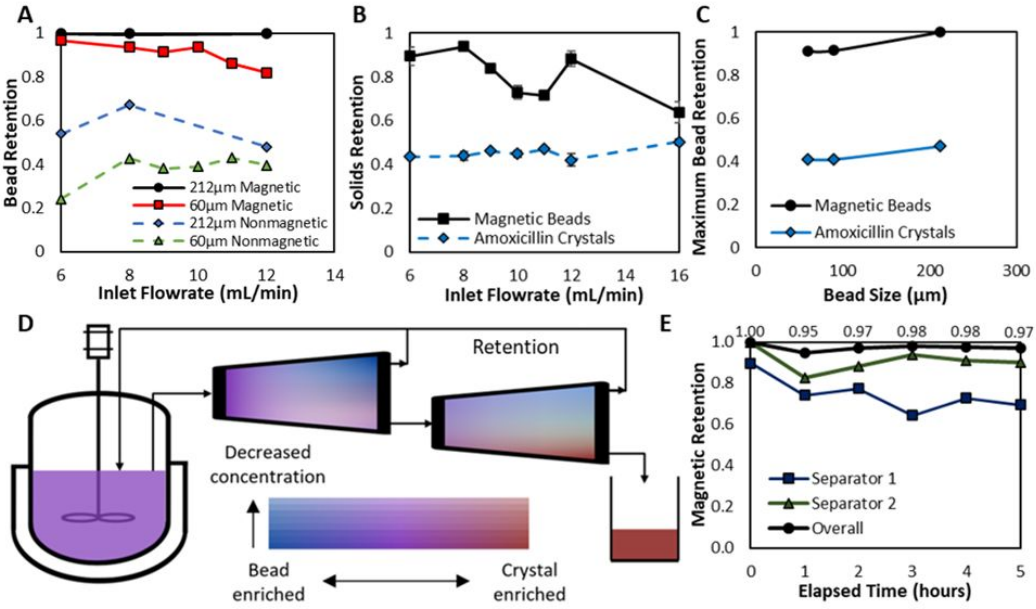

Figure 2. Testing and optimization of magnetic separation. (A) Single separator testing of bead retention during separation of magnetic and nonmagnetic beads of the same size. Both 60 µm and 212 µm beads at 10 g/L were tested to demonstrate the range of particle sizes capable of separation. Nonmagnetic particle retention is shown for the fraction of nonmagnetic beads exiting the magnetic or top outlet of the device. Error bars represent standard deviation of triplicate experiments and are smaller than the data points at all flow rates. (B) Separation of 60 µm magnetic beads from amoxicillin crystals as a function of separator inlet flow rate. Error bars show standard deviation of triplicate experiments. (C) Maximum bead retention of magnetic beads separated from amoxicillin crystals by bead size. (D) Schematic showing the setup for separators operated in series. The first separator operates at an inlet flow rate of 12 mL/min while the second device operates at 6 mL/min. The color scheme shows the anticipated crystal or bead enrichment throughout the device as well as the concentration of particles expected to exit the system. (E) Magnetic particle retention as a function of time for a 5-hour separation of 60 µm magnetic particles from amoxicillin crystals. Magnetic retention for both separators as well as the overall magnetic retention is shown.

at low inlet flow rates of 6–8 mL/min and decreased with increasing flow rate (Figure 2B). The increase in magnetic retention at an inlet flow rate of 12 mL/min compared to 10 mL/min is hypothesized to be caused by sloughing of accumulated beads below this critical flow rate. Non-spherical amoxicillin crystals seem to play a key role in bead adhesion. At < 8 mL/min, the combined bead-crystal slurry behaves the same as the bead only suspensions. Between 8 and 11 mL/min bead accumulation in the device increases, but the fluid velocity in the device is not high enough to shear beads that have accumulated outside of the designed magnetic field gradient. At 12 mL/min and above, shear forces prevent substantial bead adhesion. The non-linear relationship between separation performance and fluid flow rate depends on particle geometry, magnetic force, and viscous flow.

Devices in series were tested to improve the 60 µm magnetic bead recovery from an amoxicillin slurry beyond 90% (Figure 2D). With additional tuning (Figures S16, S17), separators in series operating at inlet flow rates of 12 mL/min and 6 mL/min separated a slurry of 60 µm magnetic particles from amoxicillin crystals while improving recovery to > 97% over the course of a 5-hour test (Figure 2E). Steady state is reached in one hour. Separation performance in series is more robust than in single devices; steady state recovery of > 97% was maintained even with perturbations to individual devices. With the addition of a magnetic trap to capture the small percentage of beads remaining in the product stream, the separation system can achieve 100% recovery of the magnetic particles. This was demonstrated for an 8-hour experiment to test scale up to continuous processing of larger slurries over longer times (Figure S18).

The final device configuration was applied to a fully continuous pilot-plant operation of the reactive crystallization of amoxicillin trihydrate (Figure 3A). Reactants 6-aminopenicillanic acid (6-APA) and 4-hydroxy-(*R*)-phenylglycine methyl ester (4-HPGME) (Scheme 1) were continuously fed into a mixed-suspension, mixed-product

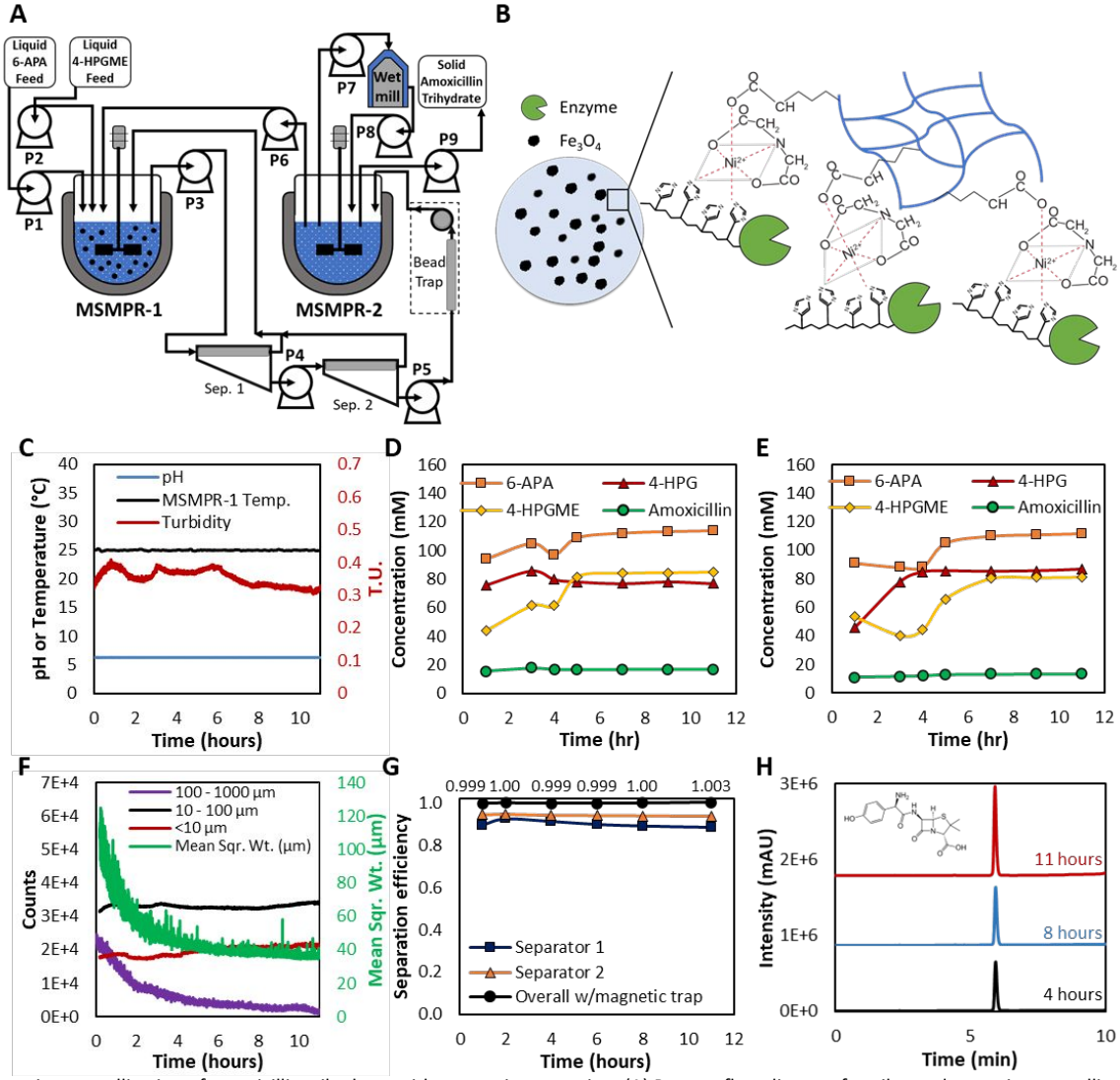

Figure 3. Reactive crystallization of amoxicillin trihydrate with magnetic separation. (A) Process flow diagram for pilot-scale reactive crystallization of amoxicillin trihydrate (B) Immobilization diagram for histidine-tagged PGA bound to magnetic agarose particles by Ni-NTA (C) pH, temperature, and turbidity data for MSMPR-1 over the course of the 11 hour pilot plant run (D) HPLC data for MSMPR-1 (E) HPLC data for MSMPR-2 (F) Crystal chord length bin counts over the 11 hour pilot run as well as the mean square weight of the crystal population. The 100 – 1000 µm counts are reported as Counts x102. (G) Separation efficiency for magnetic bead recycling sampled throughout the pilot run (H) HPLC data for solid amoxicillin trihydrate samples collected from the pilot plant run. Solid amoxicillin was dissolved in DI water prior to analysis.

removal unit (MSMPR-1) at concentrations of 240 mM and 300 mM, respectively, where their reaction to form amoxicillin is catalyzed by immobilized penicillin G acylase (PGA). Amoxicillin synthesis generates supersaturation to crystallize amoxicillin trihydrate, which protects the API from hydrolysis by PGA (Scheme 1) [16].

Efficient PGA immobilization tuning was crucial for this pilot plant operation. High PGA loading per unit of immobilized particle has been shown to have an adverse effect on β-lactam synthesis kinetics and selectivity [36]. However, for magnetic separation, increased magnetic bead concentration increases risk of clogging. Thus, catalytic and separation efficiency must be balanced. In addition, only a few commercial immobilization supports exist within the desired size range and both contain functional groups for efficient enzyme immobilization and have paramagnetic properties. Magnetic agarose particles (90 µm) containing Ni-NTA functionalization from CubeBiotech fit the criteria and were selected and tested for immobilization efficiency (Figure 3B). These particles were able to immobilize 32 mg PGA/mL bead suspension and achieve catalytic activity of 17.2 U/mg PGA. At this particle size and activity, pilot plant operation could be achieved at 13 g/L beads.

In the operation, MSMPR-1 contains a slurry of amoxicillin trihydrate crystals initially seeded at 20 g/L and 3 mL of 90 µm Ni-NTA functionalized magnetic agarose particles immobilizing 96 mg PGA in mother liquor held at pH 6.3 and 25°C (Figure 3C). The slurry of mother liquor, immobilized PGA on magnetic particles, and crystallized amoxicillin are fed through the separator system and immobilized PGA is returned to MSMPR-1. Amoxicillin trihydrate crystallizes further in MSMPR-2 at 4 °C before being collected, washed, and dried for purity analysis. The product was found to conform to USP specifications.

HPLC data were collected periodically to monitor liquid concentrations in both MSMPRs (Figures 3D and 3E). The liquid phase in each MSMPR reached steady state after approximately 5 hours. The second MSMPR was used to increase product yield by operation at 4 °C, where amoxicillin concentration was constant at its solubility of 15 mM. The solids phase, monitored by turbidity measurements (PVM; particle view monitor) and chord-length distributions (FBRM; focused beam reflectance measurements), also reached steady state after 5 hours of operation (Figures 3C and 3F). The separation system again performed well with no beads detected in final amoxicillin trihydrate product over the course of the 11-hour run (Figures 3G and 3H).

The separator system operated at > 99.9% efficiency throughout the 11-hour operation (Figure 3G). The separation efficiency of both separators decreased over time, leading to more accumulation of immobilized PGA in the magnetic trap; however, additional separators and traps can be envisioned to operate in parallel to allow for periodic cleaning without disruption of the continuous process. No magnetic beads were detected upon amoxicillin collection and the magnetic trap was periodically emptied to return immobilized PGA to MSMPR-1. Overall, 58 g of amoxicillin trihydrate was produced over 11 hours resulting in an average productivity of 253 g/L/day amoxicillin trihydrate isolated using magnetic separation of the catalyst.

4. Conclusions

A magnetic separation system, enabled by inexpensive 3D-printing, facilitated the use of immobilized penicillin G acylase (PGA) in a ~100-g scale reactive crystallization process for production of amoxicillin trihydrate. The separation system was demonstrated for particles ranging from 50 to > 200 µm and, specifically, for separation of 90-µm PGA-bound magnetic agarose particles from amoxicillin trihydrate crystals with a broad crystal size distribution. The devices were used in series for enhanced separation and a parallel implementation of the magnetic unit could be operated cyclically to allow for downtime related to potential fouling. A magnetic trap ensured catalyst-free product. At pilot-plant scale the system was demonstrated to continually produce 58 g of product in an 11-hour run using PGA bound to magnetic agarose particles, resulting in a volumetric productivity of > 250 g/L/day of amoxicillin trihydrate.

Further optimization of the device could enable use for a wider range of particle sizes by tuning the device volume, shape, and magnetic field. Nonidealities such as magnetic particle sloughing could be mitigated with use of electromagnets to tune precisely the magnetic fields generated within the device at the expense of increased energy cost. Improvements in magnetic particle technology would also enhance the separation ability of the system and increase tunability for different applications. Currently, to the best of our knowledge, only a single vendor exists for functionalized magnetic particles with > 50-µm diameter. Despite these limitations, the work detailed here serves as a proof-of-concept that can be further leveraged for other solid-solid separations.

While the device was demonstrated on enzymatic β-lactam antibiotic production routes, this approach could also be employed for process intensification of any heterogeneously catalyzed systems with a solid product. One can imagine, for example, immobilizing metal/organometallic catalysts in a similar manner for continuous solid-solid separation [48-50]. As both continuous pharmaceutical processes and reactive crystallizations are gaining traction, the design of new unit operations, including separators, is needed to accelerate the adoption of continuous, heterogeneously catalyzed reactive crystallizations and more generally expand the chemistries and processes amenable to continuous manufacturing.

Author Contributions

Conceptualization: CEL, GDM, MAM, MAG, RWR, ASB
Methodology: CEL, GDM, MAM, MAG, RWR, ASB
Investigation: CEL, GDM, MAM, PRH, MAG, RWR, ASB
Funding acquisition: MAG, RWR, ASB
Project administration: MAG, RWR, ASB
Resources: MAG, RWR, ASB
Writing – original draft: CEL, GDM, MAM, MAG, RWR, ASB
Writing – review & editing: CEL, GDM, MAM, PRH, MAG, RWR, ASB

Conflicts of interest

A patent application has been filed for the magnetic separation device technology presented in this manuscript which has been assigned U.S. Application No. 63/275,721 as of November 4th, 2021.

Acknowledgements

This work was supported by the U.S. Food and Drug Administration Center for Drug Evaluation and Research through Grant U01FD006484, which is gratefully acknowledged. C.E.L. gratefully acknowledges funding by the U.S National Science Foundation through the Graduate

Research Fellowship Program (GRFP) under Grant No. DGE-1650044.

References

1. C. L. Burcham, A. J. Florence and M. D. Johnson, *Annual Review of Chemical and Biomolecular Engineering*, 2018, **9**, 253-281.
2. B. Gutmann, D. Cantillo and C. O. Kappe, *Angewandte Chemie International Edition*, 2015, **54**, 6688-6728.
3. S. L. Lee, T. F. O'Connor, X. Yang, C. N. Cruz, S. Chatterjee, R. D. Madurawe, C. M. V. Moore, L. X. Yu and J. Woodcock, *Journal of Pharmaceutical Innovation*, 2015, **10**, 191-199.
4. M. Algorri, M. J. Abernathy, N. S. Cauchon, T. R. Christian, C. F. Lamm and C. M. V. Moore, *Journal of Pharmaceutical Sciences*, 2022, **111**, 593-607.
5. A. C. Fisher, W. Liu, A. Schick, M. Ramanadham, S. Chatterjee, R. Brykman, S. L. Lee, S. Kozlowski, A. B. Boam, S. C. Tsinontides and M. Kopcha, *International Journal of Pharmaceutics*, 2022, **622**, 121778.
6. Q. Su, S. Ganesh, M. Moreno, Y. Bommireddy, M. Gonzalez, G. V. Reklaitis and Z. K. Nagy, *Computers & Chemical Engineering*, 2019, **125**, 216-231.
7. K. P. Cole, J. M. Groh, M. D. Johnson, C. L. Burcham, B. M. Campbell, W. D. Diseroad, M. R. Heller, J. R. Howell, N. J. Kallman, T. M. Koenig, S. A. May, R. D. Miller, D. Mitchell, D. P. Myers, S. S. Myers, J. L. Phillips, C. S. Polster, T. D. White, J. Cashman, D. Hurley, R. Moylan, P. Sheehan, R. D. Spencer, K. Desmond, P. Desmond and O. Gowran, *Science*, 2017, **356**, 1144-1150.
8. A. Adamo, R. L. Beingessner, M. Behnam, J. Chen, T. F. Jamison, K. F. Jensen, J.-C. M. Monbaliu, A. S. Myerson, E. M. Revalor, D. R. Snead, T. Stelzer, N. Weeranoppanant, S. Y. Wong and P. Zhang, *Science*, 2016, **352**, 61-67.
9. M. V. Hernando, J. C. Moore, R. A. Howie, R. A. Castledine, S. L. Bourne, G. N. Jenkins, P. Licence, M. Poliakoff and M. W. George, *Organic Process Research & Development*, 2022, **26**, 1145-1151.
10. W. J. Liu, C. Y. Ma, J. J. Liu, Y. Zhang and X. Z. Wang, *AIChE Journal*, 2017, **63**, 967-974.
11. J. Neuburger, F. Helmholz, S. Tiedemann, P. Lehmann, P. Süss, U. Menyes and J. von Langermann, *Chemical Engineering and Processing - Process Intensification*, 2021, **168**, 108578.
12. L. Rogers, N. Briggs, R. Achermann, A. Adamo, M. Azad, D. Brancazio, G. Capellades, G. Hammersmith, T. Hart, J. Imbrogno, L. P. Kelly, G. Liang, C. Neurohr, K. Rapp, M. G. Russell, C. Salz, D. A. Thomas, L. Weimann, T. F. Jamison, A. S. Myerson and K. F. Jensen, *Organic Process Research & Development*, 2020, **24**, 2183-2196.
13. R. Singh, C. Velazquez, A. Sahay, K. M. Karry, F. J. Muzzio, M. G. Ierapetritou and R. Ramachandran, in *Process Simulation and Data Modeling in Solid Oral Drug Development and Manufacture*, eds. M. G. Ierapetritou and R. Ramachandran, Springer New York, New York, NY, 2016, DOI: 10.1007/978-1-4939-2996-2_7, pp. 191-224.
14. C.-H. Ho, J. Yi and X. Wang, *ACS Sustainable Chemistry & Engineering*, 2019, **7**, 1038-1051.
15. L. G. Encarnación-Gómez, A. S. Bommarius and R. W. Rousseau, *Reaction Chemistry & Engineering*, 2016, **1**, 321-329.
16. M. A. McDonald, A. S. Bommarius, M. A. Grover and R. W. Rousseau, *Computers & Chemical Engineering*, 2019, **126**, 332-341.
17. M. A. McDonald, A. S. Bommarius and R. W. Rousseau, *Chemical Engineering Science*, 2017, **165**, 81-88.
18. M. A. McDonald, A. S. Bommarius, R. W. Rousseau and M. A. Grover, *Computers & Chemical Engineering*, 2019, **123**, 331-343.
19. M. A. McDonald, H. Salami, P. R. Harris, C. E. Lagerman, X. Yang, A. S. Bommarius, M. A. Grover and R. W. Rousseau, *Reaction Chemistry & Engineering*, 2021, **6**, 364-400.
20. M. Doeker, L. Grabowski, D. Rother and A. Jupke, *Green Chemistry*, 2022, **24**, 295-304.
21. S. Amari, C. Sugawara, R. Harada, S. Kudo and H. Takiyama, *Chemical Engineering Research and Design*, 2021, **176**, 116-122.
22. O. Fellechner, M. Blatkiewicz and I. Smirnova, *Chemie Ingenieur Technik*, 2019, **91**, 1522-1543.
23. C. Hu, B. T. Shores, R. A. Derech, C. J. Testa, P. Hermant, W. Wu, K. Shvedova, A. Ramnath, L. Q. Al Ismaili, Q. Su, R. Sayin, S. C. Born, B. Takizawa, T. F. O'Connor, X. Yang, S. Ramanujam and S. Mascia, *Reaction Chemistry & Engineering*, 2020, **5**, 1950-1962.
24. S. L. M. Janbon, A. R. Parsons, E. Gavi and G. K. Reynolds, *Organic Process Research & Development*, 2019, **23**, 302-308.
25. M. Jiang and X.-W. Ni, *Organic Process Research & Development*, 2019, **23**, 882-890.
26. M. F. Jiang and X. W. Ni, *Journal of Crystal Growth*, 2019, **523**, 7.
27. W. J. Liu, C. Y. Ma and X. Z. Wang, *Procedia Engineering*, 2015, **102**, 499-507.
28. N. M. Nikačević, A. E. M. Huesman, P. M. J. Van den Hof and A. I. Stankiewicz, *Chemical Engineering and Processing: Process Intensification*, 2012, **52**, 1-15.
29. M. Purwins, A. Weber, P. Berwian, G. Müller, F. Hergert, S. Jost and R. Hock, *Journal of Crystal Growth*, 2006, **287**, 408-413.
30. W. Su, Y. Jiang, X. Zuo, C. Li and H. Wang, *Chemical Engineering Journal*, 2022, **431**, 134186.
31. S. Teychené, I. Rodríguez-Ruiz and R. K. Ramamoorthy, *Current Opinion in Colloid & Interface Science*, 2020, **46**, 1-19.
32. M. D. Truppo, *ACS Medicinal Chemistry Letters*, 2017, **8**, 476-480.
33. M. P. Thompson, I. Peñafiel, S. C. Cosgrove and N. J. Turner, *Organic Process Research & Development*, 2019, **23**, 9-18.
34. H. Salami, P. R. Harris, D. C. Yu, A. S. Bommarius, R. W. Rousseau and M. A. Grover, *Chemical Engineering Research and Design*, 2022, **177**, 473-483.
35. P. Valencia, S. Flores, L. Wilson and A. Illanes, *Appl Biochem Biotechnol*, 2011, **165**, 426-441.
36. H. Salami, C. E. Lagerman, P. R. Harris, M. A. McDonald, A. S. Bommarius, R. W. Rousseau and M. A. Grover, *Reaction Chemistry & Engineering*, 2020, **5**, 2064-2080.
37. M. Frenea-Robin and J. Marchalot, *Magnetochemistry*, 2022, **8**, 11.
38. M. Zborowski and J. J. Chalmers, *Analytical Chemistry*, 2011, **83**, 8050-8056.
39. Y. Haik, V. Pai and C.-J. Chen, *Journal of Magnetism and Magnetic Materials*, 1999, **194**, 254-261.

40. L. Borlido, A. M. Azevedo, A. C. A. Roque and M. R. Aires-Barros, *Biotechnology Advances*, 2013, **31**, 1374-1385.
41. J. Oberteuffer, *IEEE Transactions on Magnetics*, 1974, **10**, 223-238.
42. E. C. H. T. Lau and H. H. P. Yiu, in *Nanomaterials for Biocatalysis*, eds. G. R. Castro, A. K. Nadda, T. A. Nguyen, X. Qi and G. Yasin, Elsevier, 2022, DOI: https://doi.org/10.1016/B978-0-12-824436-4.00001-0, pp. 301-321.
43. V. G. Matveeva and L. M. Bronstein, *Nanomaterials (Basel)*, 2021, **11**.
44. S. P. Vibhute, P. M. Mhaldar, R. V. Shejwal and D. M. Pore, *Tetrahedron Letters*, 2020, **61**, 151594.
45. C. González-Fernández, J. Gómez-Pastora, E. Bringas, M. Zborowski, J. J. Chalmers and I. Ortiz, *Industrial & Engineering Chemistry Research*, 2021, **60**, 16780-16790.
46. C. Mikkelsen and H. Bruus, *Lab on a Chip*, 2005, **5**, 1293-1297.
47. C. B. Fuh, M. H. Lai, L. Y. Lin and S. Y. Yeh, *Analytical Chemistry*, 2000, **72**, 3590-3595.
48. M. M. Hansen, D. J. Jarmer, E. Arslantas, A. C. DeBaillie, A. L. Frederick, M. Harding, D. W. Hoard, A. Hollister, D. Huber, S. P. Kolis, J. E. Kuehne-Willmore, T. Kull, M. E. Laurila, R. J. Linder, T. J. Martin, J. R. Martinelli, M. J. McCulley, R. N. Richey, D. R. Starkey, J. A. Ward, N. Zaborenko and T. Zweifel, *Organic Process Research & Development*, 2015, **19**, 1214-1230.
49. T. A. Martinot, B. C. Austad, A. Côté, K. M. Depew, D. Genov, L. Grenier, J. Helble, A. Lescarbeau, S. Nair, M. Trudeau, P. White and L.-C. Yu, *Organic Process Research & Development*, 2015, **19**, 1693-1702.
50. J. Yin, M. Weisel, Y. Ji, Z. Liu, J. Liu, D. J. Wallace, F. Xu, B. D. Sherry and N. Yasuda, *Organic Process Research & Development*, 2018, **22**, 273-277.